Journal of Photochemistry, 10 (1979) 77 - 110

THE PHYSICS AND CHEMISTRY OF SOLAR CELLS*

K. W. BÖER

College of Engineering, University of Delaware, Newark, Del. 19711 (U.S.A.) and SES Inc., Newark, Del. 19711 (U.S.A.)

(Received August 10, 1978)

Summary

The physics of the photovoltaic effect is analyzed using the example of a frontwall solar cell. The effect results from the interplay of the emitter, in which minority carriers are generated via absorbed light and diffuse to the junction, and the junction, in which the essential voltage drop occurs. The interplay is established by the minority carrier density at the emitter–junction interface, acting as prominent boundary condition, and connecting current through the device with applied voltage.

The chemistry of the interlayer between emitter and junction has essential influence on this boundary condition by determining interface recombination and space charge. Both of these determine band connection and performance of the device.

A brief review of material properties in the light of the basic cell operation is given.

1. Introduction

The physics of solar cells describes the photovoltaic effect in inhomogeneous materials in terms of generation of electron–hole pairs, trapping, recombination and transport of these carriers throughout the semiconducting material and into the electrodes.

The chemistry of solar cells deals with the material and its specific inhomogeneities and includes defect chemistry, *i.e.* deviation from stoichiometry and doping, mostly in non-equilibrium conditions.

A solar cell contains at least two active parts, the emitter and the junction. In the emitter most of the light is absorbed creating electron–hole pairs and in the junction electrons and holes are separated from each other and

*Paper presented at the Second International Conference on the Photochemical Conversion and Storage of Solar Energy, Cambridge, August 1978.

may recombine through an external circuit causing the flow of a photoelectric current.

It is generally accepted that minority carriers, generated by light and diffusing to the junction, are responsible for the current in a photovoltaic cell, and that the voltage drop across the junction accounts for the desired fraction of the voltage drop across the cell.

However, the complexity of the physical model, involving the transport equations of both carriers and the Poisson equation with explicit spatial coordinates, has caused most researchers in the past to shy away from a systematic discussion of the physics of the photovoltaic cell, except for a few specific discussions of isolated problems. Such discussions were mainly related to the minority carrier diffusion, collection efficiency, quasi-Fermi level analysis with the aim of estimating the open circuit voltage, and certain recombination phenomena in the junction region which seem to influence the current–voltage characteristics [1 - 4]. Only recently has more effort been devoted to the discussion of the spatial distribution of space charge, the field and the potential in the junction region [5, 6].

None of the early discussions of a physical model yielded a current–voltage characteristic of solar cells. For this, usually an electrotechnical model was used, describing the solar cell as a diode in parallel with a current generator, having the effect of a parallel shift of the diode characteristic by the short circuit.

However, mathematically such a parallel shift is not permissible since the solutions of a non-linear system of differential equations (*i.e.* the transport and Poisson equations) do not transform linearly [6].

Moreover, the mostly used adjustment parameters (to obtain improved agreement with the experiment), when explained as shunt and series resistance and as exponential correction factor (indicating the type of junction recombination), may in fact be misleading[a] since similar curve shapes may be obtained for entirely different reasons [7].

Therefore an attempt was made to develop a self-consistent physical theory of the current–voltage characteristics [5, 8]. Necessary simplifications (without distorting any of the prominent features of the characteristics) are most easily introduced for an abrupt heterojunction in frontwall cells and hence were initially introduced for the example of CdS/Cu_2S solar cells [5 - 10] which are believed to have such an abrupt heterojunction.

However, in the following discussion we shall broaden the analysis to include homojunctions and heterojunctions of frontwall[b] cells.

We shall first identify the main parts of a photovoltaic cell and define their operational properties. We shall then describe quantitatively the operation of each part and finally develop the current–voltage characteristics by

---

[a] In fact results obtained from an incorrect theory cannot be corrected by a correct model modification if one expects meaningful results indicative of the parameter of the model modification.

[b] In backwall cells both carriers must be considered within the junction, hence rendering the discussion more complex (see footnote on page 84 and ref. 45).

joining the different parts of the cell, with major attention to the pertinent boundary conditions between these parts.

In deriving these characteristics it becomes evident that not only the chemistry of emitter, junction and collector are of importance but (clearly identifiable at abrupt heterojunctions) the chemistry of interfaces is key to the electrical behavior of such cells. Commonly such interface layers are neglected (except for Schottky barrier cells where the interlayer between the metal electrode and the active semiconductor is already identified as being of major importance). One often resorts to the discussion of differences of work functions (or electron affinities) and of the lattice mismatch as the only tools for junction interface discussion — and mostly with unsatisfactory quantitative results.

We shall therefore try to develop a microscopic model including the chemistry of the interface layer to obtain quantitative results. Because of the large variety of chemical possibilities we shall specifically discuss the $Cd_zZn_{1-z}S$–Cu_2S solar cell as an example of the given theory.

Other material combinations will be discussed briefly in the light of the main presentation.

2. Main parts of the solar cell

A solar cell has two active parts, the emitter and the junction, and three classes of passive parts, the semiconductive assist-layers (as defined below), the electrodes and the window/encapsulant. Dependent on the type of solar cell (frontwall, backwall, Schottky junction etc.) one or more of these layers may be combined with others or may be omitted. The following listing gives a general overview of these layers and their main purposes in the operation of the cell.

2.1. Active parts

The *emitter* absorbs most of the light, generating minority carriers, and permits diffusion[a] of these carriers to or from the junction. The magnitude and sign of the diffusion current is determined by the minority carrier density at the emitter-to-junction interface. The chemistry of the emitter determines the minority carrier lifetime and hence the limit of the current (saturation current).

The majority current in the emitter is carried by drift (since the majority carrier density–mobility product is usually orders of magnitude larger than that of minority carriers).

The *junction* provides almost all of the voltage drop of the cell. The voltage drop which occurs in other parts of the cell contributes mostly to the undesired series resistance (except for drift fields near surfaces and restricted to a small fraction of the emitter). In the junction, the minority carriers created

[a] Diffusion rather than drift is the main cause of the photovoltaic current.

in the emitter are effectively separated from the emitter and, with sufficient reverse bias, can only return to the emitter through the external circuit.

An *interface layer* may exist between emitter and junction (or may be a small part thereof) in which the defect density is substantially larger[a] than in the adjacent layers, and major space charges and/or major carrier recombination occur. Space charge and recombination influence potential and current distribution (see Section 3.2).

2.2. Semiconductive assist-layers

A semiconductive *collector* layer may extend from the junction interface opposite the emitter to the collector electrode. This collector layer provides the space for expansion of the junction with increasing reverse bias (in frontwall cells).

A *surface passivation layer* on the emitter, opposite the junction, is occasionally applied to reduce surface recombination. The passivation layer may be created by heavy doping (*e.g.* p^+ on p in Si homojunction cells) or, preferably, by heterojunction windows ($Ga_xAl_{1-x}As$ on GaAs or Cu_2O on Cu_2S).

A *current-assist* conductive and transparent top coating may be applied in order to reduce lateral current densities, hence allowing lesser doping of the front semiconductive layer and therefore permitting increased minority carrier lifetime (if this layer is the emitter) or a thinner less optically absorbing layer (if this layer is the collector).

2.3. Electrodes

The *grid* (front) *electrode* must permit sufficient light penetration and at the same time allow current collection without major series resistance limitation. Proper gridline spacing and geometry and intimate gridline contact is required to avoid excessive lateral current densities.

The *back electrode* is usually massive metal layer with "ohmic" contact properties, often acting as part of the encapsulation. Multilayers of different metals may be used to fulfill mechanical, chemical and electrical needs.

2.4. Window/encapsulant

Single or multi-layer *optical coatings* may fulfill a multitude of needs, such as mechanical support of grids, antireflecting coatings and hermetic seal to block penetration of active gases to the semiconductor and/or metal surface, hence preventing photochemical surface reactions and corrosion.

---

[a]Such an interface layer may be caused for example by a lattice mismatch in the heterojunction or by doping compensation causing substantial donor–acceptor pair formation.

3. Cell operation

3.1. Emitter

An effective emitter absorbs most of the light, generating a substantial increase in minority carrier density (for definiteness here assumed to be electrons)[a]:

$$n_{10} = g\tau_n \tag{1}$$

(index 1 refers to the emitter, index 0 to the bulk (here of the emitter) neglecting surface effects), g is the (for calculations in Section 3.1.1. assumed homogeneous)[b] generation rate and τ_n is the minority carrier lifetime.

Electrons generated in the emitter may recombine in the bulk (characterized by τ_n), diffuse to the surface and recombine here (characterized by the surface recombination velocity s) or diffuse to the junction (see below).

3.1.1. Diffusion current

Key to the understanding of the operation of the photovoltaic cell is the fact that the diffusion of the electrons to (or from) the junction is determined by the electron density n_j at the emitter–junction interface[c] (boundary condition in the mathematical sense). If n_j is lower than n_{10}, electrons diffuse from the emitter bulk to the junction with a diffusion current which is the larger the lower n_j is (reverse bias). However, one should remember that n_j is limited by the Richard–Dushman emission [3] and hence cannot decrease below $(6\pi)^{1/2} j_n/ev_n$. If n_j is larger than n_{10} electrons diffuse from the junction into the emitter (forward bias).

The diffusion current

$$j_n = \mu kT \frac{dn}{dx} \tag{2}$$

can be calculated for

$$n(x) = \tau_n \left(g + \frac{1}{e} \frac{\partial j_n}{\partial x} \right) \tag{3}$$

yielding[d] [9]

---

[a] Better solar cells indeed have a p-type emitter, since the $\mu_n n$ product is usually larger than $\mu_p p$ for the same material.

[b] This assumption is used here to obtain a simple solution of the diffusion equation. This causes a lesser error than the often used exponential dependence of g on x [9].

[c] This interface is rather well defined in some abrupt heterojunction, *e.g.* as the interface between CdS and Cu_2S in the CdS–Cu_2S heterojunction, but needs to be defined in other solar cells. We shall attempt a general definition in Section 3.2.

[d] In the given form, using x_m, the lengthy expression obtained [9] by solving eqns. (2) and (3) is hidden in the tanh term. Equation (4) shows, in a rather transparent way, the dependence of j_n on n_j.

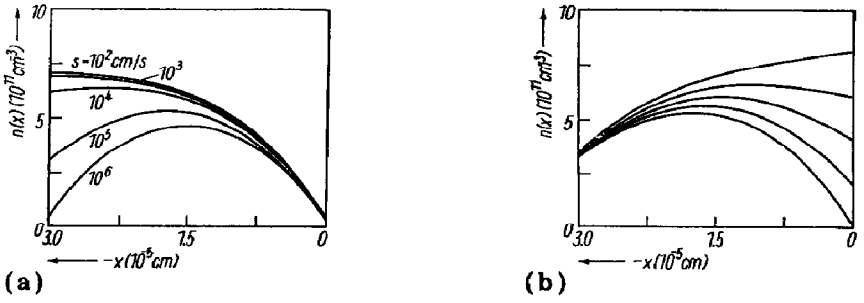

Fig. 1. Electron density profile in the emitter for $L_n = 10^{-5}$ cm, $g\tau_n = 7.5 \times 10^{11}$ cm^{-3} and s or j_n as family parameters in (a) and (b) respectively. $s = 10^5$ cm s^{-1} in (b).

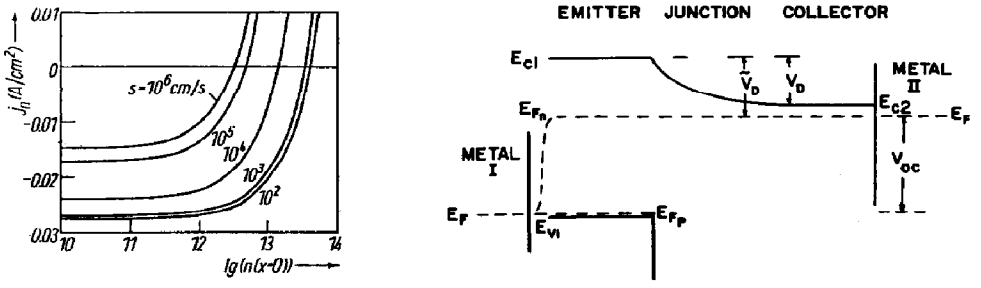

Fig. 2. Electron current density at $x = 0$ as a function of ln n_j for s as family parameter, $L_n = 7.5 \times 10^{-5}$ cm and $g = 6 \times 10^{21}$ cm^{-3} s^{-1}.

Fig. 3. Simple band model of a heterojunction with minority carrier generation in the emitter, but neglecting interface recombination at the emitter–junction interface or marked recombination influence of E_{Fp} at the emitter–metal interface.

$$j_n(x = 0) = e \frac{L_n}{\tau_n} (n_j - n_{10}) \tanh\left(\frac{x_m}{L_n}\right) \tag{4}$$

($x = 0$ and $x = -d_1$ are the position of the junction interface and the emitter surface respectively), L_n is the diffusion length of electrons and x_m is the position of the electron density maximum in the emitter in reverse bias. x_m depends on surface recombination and bias, but is typically of the order of $0.5d_1$ (Fig. 1).

For better photovoltaic cells, L_n is substantially (at least by a factor of 2) larger than d_1. Neglecting detail (for such see ref. 9) eqn. (4) can be simplified to

$$j_n(x = 0) = e \frac{x_m}{\tau_n} (n_j - n_{10}) \tag{5}$$

and x_m may be replaced by d_1 for negligible surface recombination.

The relation of this current to typical current–voltage characteristics of solar cells becomes obvious when j_n of eqns. (4) or (5) is plotted as a function

of ln n_j (Fig. 2). A current–voltage characteristic can be derived from this plot if ln n_j can be related to the applied voltage. This is indeed possible as shown in Section 3.2.1.

3.1.2. Open circuit voltage

In order to obtain the pertinent relation to the applied voltage, the various contributions to the voltage drop across the cell need to be evaluated.

The main[a] voltage drop is best divided into two parts: the open circuit voltage and the additional voltage drop in the junction when current flows.

Neglecting interface recombination[b] the open circuit voltage is identical to the separation of the two quasi-Fermi levels in the emitter (Fig. 3):

$$V_{oc} = \frac{1}{e}\{E_{g1} - (E_{c1} - E_{Fn}) - (E_{Fp} - E_{v1}) - \delta E_{g1}\} \tag{6}$$

where E_{g1} is the band gap of the emitter and δE_{g1} the narrowing of this gap at high doping levels. With

$$E_{c1} - E_{Fn} = \frac{kT}{e} \ln\left(\frac{N_{c1}}{g\tau_n}\right) \tag{7}$$

the well-known logarithmic dependence of V_{oc} on the generation rate is explained ($E_{Fp} - E_{v1}$ and δE_{g1} are essentially independent of g).

3.2. Junction

The voltage drop within the junction is best related to open circuit conditions. At open circuit voltage, it is the diffusion voltage:

$$V_D = \frac{kT}{e} \ln\left(\frac{n_{20}}{n_{10}}\right) \tag{8}$$

3.2.1. Applied voltage

When applying a voltage to the cell that is different from the open circuit voltage, a current will flow and a voltage different from the diffusion voltage will occur across the junction:

$$V_j = V_D + (V_{appl} - V_{oc}) \tag{9}$$

In contrast to common practice, we shall label the applied voltage in reference to the open circuit voltage, and refer to a forward bias when $V_{appl} - V_{oc} > 0$ and to a reverse bias when $V_{appl} - V_{oc} < 0$. This provides a current relation in the junction similar to that in an unilluminated diode.

---

[a] Neglecting any voltage drop caused by series resistances.

[b] Obviously, neglect of interface recombination usually results in a larger than observed open circuit voltage and sometimes a different slope of V_{oc} *versus* g and/or T (we shall return to this problem in Section 3.4).

The voltage drop across the junction is consequently calculated from the solution of the transport equation (where for simplicity we have neglected the hole transport equation):

$$j_n = e\mu nF - \mu kT \frac{dn}{dx} \tag{10a}$$

and the Poisson equation

$$\frac{dF}{dx} = \frac{e}{\epsilon\epsilon_0}\rho(n, x) \tag{10b}$$

with

$$F = -\frac{dV}{dx} \tag{10c}$$

and requires in addition to the boundary condition n_j, as mentioned in Section 3.1, two others for F and V. We shall return to these in Section 3.4.

3.2.2. Solution near V_{oc}

For j_n much smaller than the drift or diffusion current (Boltzmann range), the solution of eqns. (10) is easily given:

$$n = n_{20} \exp\left\{-\frac{eV(x)}{kT}\right\} \tag{11}$$

yielding

$$n(x = 0, j_n \approx 0) = n_{20} \exp\left(-\frac{eV_j}{kT}\right) \tag{11a}$$

or

$$V_{app} = V_{oc} + \frac{kT}{e} \ln\left(\frac{n_j}{n_{10}}\right) \tag{12}$$

Equation (12) indeed relates ln n_j to the applied voltage, as suggested from the discussion of Fig. 2 in Section 3.1, and yields when combined[a] with eqn. (4)

$$j_n = e\frac{L_n n_{10}}{\tau_n}\left[\exp\left\{-\frac{e(V_{appl} - V_{oc})}{kT}\right\} - 1\right] \tanh\left(\frac{x_m}{L_n}\right) \tag{13}$$

[a] Such a combination is justified for frontwall cells where the highly doped emitter changes rapidly into the much less doped junction and the minority carrier density of the emitter consequently becomes the majority carrier density of the junction "at" the emitter–junction interface.

which may be rewritten as the well-known current–voltage relation for ideal photovoltaic cells

$$j_n = j_{00} \exp\left(-\frac{e\phi}{kT}\right) \exp\left(\frac{eV_{appl}}{kT}\right) - j_s \tag{13a}$$

although with somewhat modified parameters

$$j_{00} = e\frac{L_n}{\tau_n} N_{c2} \tanh\left(\frac{x_m}{L_n}\right) \tag{13b}$$

$$\phi = \tilde{V}_D + V_{oc} \tag{13c}$$

$$\tilde{V}_D = \frac{kT}{e} \ln\frac{N_{c2}}{n_{10}} \tag{13d}$$

$$j_s = e\frac{L_n}{\tau_n} n_{10} \tanh\left(\frac{x_m}{L_n}\right) = eL_n g \tanh\left(\frac{x_m}{L_n}\right)^{a} \tag{13e}$$

Equations (13) show a much improved agreement with the experiment, since j_{00} is several orders of magnitude smaller than in previous theories[b] and the measured ϕ is indeed within the experimental error equal to the sum of the measured V_{oc} and $\tilde{V}_D$ (see Section 5).

It should also be recognized that ϕ in the given theory has no other meaning than that shown in eqn. (13c) and is not to be confused with a barrier height for electron transport in reverse direction (such a barrier height is indeed $\tilde{V}_D$ and not ϕ — see Fig. 3).

3.2.3. Current–voltage characteristics

It should, however, be remembered that eqn. (13) holds only for the Boltzmann range, *i.e.* near the open circuit voltage, and not for the entire current–voltage characteristic. For values of the applied voltage more than a few kT/e from V_{oc} eqns. (10) need to be integrated properly; hence we need to know more about the defect distribution in the junction and its influence on the space charge development with widening (reverse bias) or shrinking (forward bias) of the junction region. For each point of the characteristic, j_n enters as the parameter in the transport equation. Numerical integration can be accomplished for any given model, and the result is shown for an

---

[a] Current saturation may be limited before the value given in eqn. (13e) is reached by a high-field domain in the junction. This effect is described elsewhere [5, 6] and is not the subject of this paper.

[b] $j_{00} = ev_n N_c$, where v_n is the r.m.s. electron velocity, for the classical diffusion theory or $j_{00} = e\mu F_c N_c$, where F_c is the junction field, for the drift theory of the junction [10].

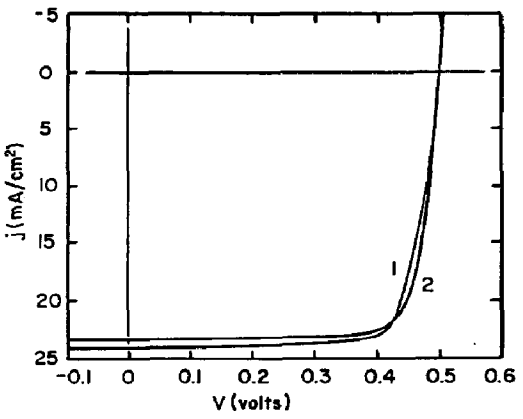

Fig. 4. Current–voltage characteristics calculated by integrating eqns. (10) with eqn. (4) supplying the boundary condition with $\rho_{max} = 4 \times 10^{15}$ (curve 1) and 1.6×10^{15} (curve 2).

example in Fig. 4. The shape of the current–voltage characteristic obtained depends on the junction model (defect distribution in the junction) chosen and is not the subject of this paper.

3.3. Interface layer

For most photovoltaic devices, the agreement between the given theory and experiment is not yet satisfactory because a major factor in these devices was neglected, namely interface recombination. Let us now assume that such interface recombination plays a *dominant* role. In contrast to some initial belief this will *not* render such a photovoltaic device ineffective, but usually only reduce the open circuit voltage and/or the short circuit current (see Section 4.5).

This somewhat unexpected result is based on the fact that interface recombination and minority carrier "leakage" through the junction interface into junction and collector are competing processes, and the latter may be impeded by a potential spike, the height and width of which are dependent on the density of interface states.

3.3.1. Negligible interface recombination

In order to understand this behavior, let us first analyze the current distribution in the emitter without interface recombination.

For current saturation, the electron density profile is similar to the upper curve in Fig. 1(a). Consequently, the electron current increases (almost linearly, as shown in ref. 9) with decreasing distance from the junction interface. For reasons of total current continuity ($j_n + j_p = j$ = constant) the hole current must decrease accordingly. Since the hole density is much larger than the electron density in the collector, such a hole current profile can be achieved by a very small field (Fig. 5) which easily self-adjusts by a small space charge of about 10^8 cm^{-3} in the example of Fig. 5 (for $d_1 \approx 2 \times 10^{-5}$ cm and $\epsilon \approx 10$). Hence, at the outer surface (assumed to be covered with a transparent electrode) the entire current is carried by hole

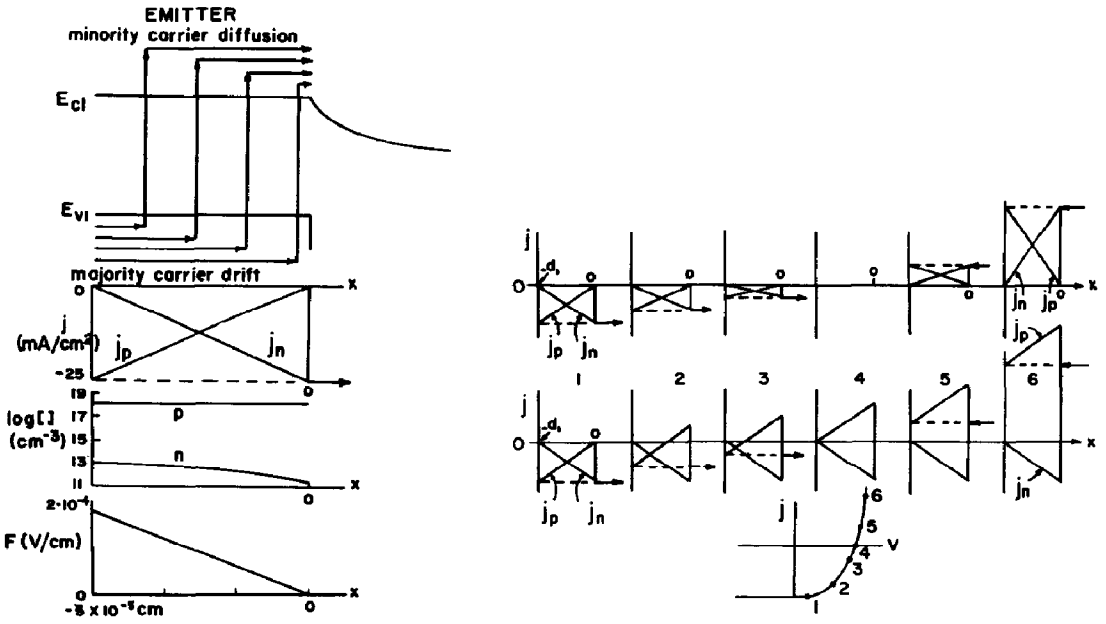

Fig. 5. Current, carrier density and field profile in the collector at saturation current (reverse bias) with no surface recombination. Upper graph: simplified band model with current schematics.

Fig. 6. Current distribution $j_n(x)$ and $j_p(x)$ in the collector at six different points of the current–voltage characteristics as shown in the lower insert. Upper row: zero interface recombination. Lower row: dominant interface recombination. Arrow indicates direction of electron current. Lower insert: j–V characteristic depicting the six cases shown above.

drift which changes via minority carrier generation into electron (diffusion) current with increasing distance from the outer surface (upper two graphs of Fig. 5). At the junction interface the hole current has finally vanished and the entire current is carried by electron diffusion.

Figure 6 shows the current distribution for six different currents as indicated in the characteristic shown in the lower insert. Case 1 reproduces the second part of Fig. 5. The upper row assumes zero interface recombination. Upper and lower rows have negligible surface ($x = -d_1$) recombination.

We discuss first the upper row. With increased applied voltage (lower reverse bias) (cases 2 and 3) the distributions remain similar; however, the slopes are reduced.

For the open circuit condition (case 4) the minority carrier density does not change with x, there is no diffusion current and hence $j_n = j_p = 0$ throughout the entire collector.

In forward bias (cases 5 and 6), the signs of both j_n and j_p are reversed. However, the electron current is again largest at the junction interface and zero at the outer emitter surface. The current reverts from electron diffusion to hole drift by bulk recombination. Even though the slopes of j_n and j_p must add up to 180° at each x, the behavior shown in cases 5 and 6 is one example of recombination, extending over the entire emitter evenly. A wide variety of other recombination distributions is possible.

3.3.2. Dominant interface recombination

With dominant interface recombination (lower row of Fig. 6) let us start discussing the open circuit condition first (case 4). Here zero current is achieved by an electron and hole current flowing in the same direction (*i.e.* opposite in sign) and hence cancelling each other. Here both currents increase linearly when approaching the interface. These currents are caused by major interface recombination.

In reverse bias, the electron current profile in the emitter remains unchanged. Dominant interface recombination always draws the maximum possible electron (diffusion) current towards the junction interface. However, lowering the electron density at the junction side of the interface (at $x = 0^+$) causes electrons to leak out from the emitter and produces a net current into the junction. This net current can (at best) be (almost) equal to the electron current at $x = 0^-$ and requires a shift of the triangular hole current downwards with essentially no remaining recombination (hole) current at the interface as shown in case 1. Reverse currents before saturation are shown as cases 2 and 3.

In forward bias, excess electrons at the junction interface recombine here and hence shift the hole current upward (cases 5 and 6) while again leaving the electron current in the emitter unchanged.

It is therefore indicated that, in contrast to the case of negligible interface recombination, where the *change in electron current* at the interface produced the net current with dominant interface recombination the *change in hole current* causes the change in net current. As seen from the lower row of Fig. 6, such a change in hole current is accomplished by a shift of the hole current at the interface. Since holes can easily be supplied from the electrode but not from the junction through the interface (in the given example of a p-type emitter) the sequence from cases 6 - 1 must stop at 1 (decreasing $j_p(x = 0)$ with $j_p(x = 0) = 0$ for case 1). This again causes current saturation.

3.4. Interface boundary conditions

As shown in Sections 3.1. and 3.2. for *zero interface recombination*, the interface boundary condition n_j connects the current flow from the emitter and the voltage drop in the junction: n_j was given by eqn. (4) as a function of the electron current at the junction interface. n_j is also the boundary condition for integration of eqn. (10a). The other boundary conditions are the field F_j and the potential $-V_j$ at the junction interface ($V = 0$ is assumed at the collector electrode). In order to obtain the yet unknown boundary conditions F_j and V_j we may first start integration of eqn. (10) from the collector bulk towards the emitter junction interface. Since the solution approaches a singular point ($dF/dx = dn/dx = 0$) in the collector bulk, a boundary condition close to n_{20} and F_{20} given by $j = j_n = e\mu n_{20}F_{20}$, such as $n_{20} - \delta n$ and $F_{20} + \delta F$ with $\delta n \ll n_{20}$ and $\delta F \ll F_{20}$ may be chosen with the numerical integration proceeding towards the junction. F_j and V_j can then be obtained from the obtained $F(x)$ and $V(x)$ at the position x at which $n(x) = n_j$.

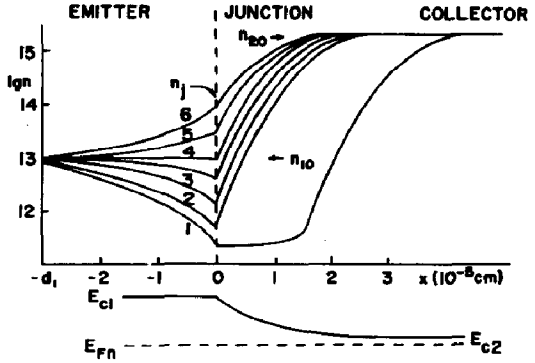

Fig. 7. Electron density profile (at the edge of the conduction bands) in emitter, junction and collector for different bias (currents). The family numbering refers to the same set of numbers in Fig. 4. The lower diagram depicts conduction band and electron-quasi-Fermi level of such a junction in open circuit condition.

The electron density distribution for a photovoltaic cell with negligible interface recombination is schematically illustrated in Fig. 7 for a variety of bias conditions; the numbers indicate conditions similar to those given in Fig. 6, clearly illustrating the double role of n_j as connecting boundary condition for emitter and junction. In the lower part of Fig. 7, conduction band and quasi-Fermi levels are shown for open circuit condition.

For *dominant interface recombination*, this condition must be re-evaluated. As shown in the lower row of Fig. 6, the electron density distribution in the emitter remains essentially the same independent of bias; hence n_j is not a boundary condition for the emitter. However, since $n(x)$ was fixed in the emitter by interface recombination, which is an effect of importance for photogenerated carriers but not for thermally generated carriers, we expect that, by introducing such interface recombination, few changes[a] will occur in the junction and collector, in which photogeneration is negligible.

As a consequence for all but current saturation, n_j shows a jump with $n(x = 0^-) < n(x = 0^+)$ (Fig. 8). It should be recognized that in Fig. 8 the electron densities at the lower edge of the conduction bands are plotted, hence the jump. When drawn for any $n_j(E)$ at the same energy, at open circuit condition most of the jump disappears except for the difference in density of states in emitter and junction. In reverse bias, however, for any given energy, the electron density at $x = 0^+$ is smaller than at $x = 0^-$, providing the driving force for the current (the inverse holds for forward bias). The band diagram shown for open circuit condition in the lower part of Fig. 8 illustrates the reason for the jump: the quasi-Fermi level for electrons is lowered in the emitter near the junction. However, since the electron distribution in junction and collector remain the same as without interface recombination, E_{Fn2} and $E_{c2}(x)$ slide down by the same amount: $E_{Fn10} - E_{Fn1}(x = 0^-)$. Hence E_c experiences a jump at the interface of the same amount:

[a]The electron density, which is shown to be continuous at the interface in Fig. 7, is actually discontinuous for reasons of different density of states in the conduction bands of both materials. In Fig. 8 this effect is even larger causing partial reflection of electrons when passing through the interface. However, this effect is neglected in this paper.

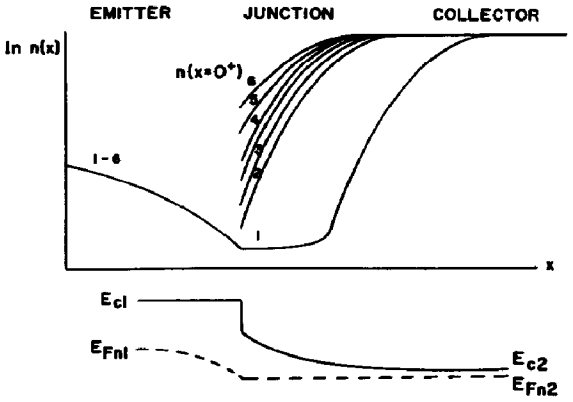

Fig. 8. Electron density profile and band scheme similar to Fig. 7, but for dominant interface recombination. (Attention: continuity of curves (1 - 6)/1 does not imply continuity in $E_c(x)$ at $x = 0$. The quasi-Fermi level for electrons is also discontinuous at $x = 0$ for $j_n \neq 0$ in order to provide for the necessary driving force.)

$$\Delta E_c = E_{c1}(x = 0^-) - E_{c2}(x = 0^+) = kT \ln (n_{2jR0}/n_{1jR0}) \tag{14}$$

with $n_{1jR0} = n_j(x = 0^-, j = 0)$ and $n_{2jR0} = n_j(x = 0^+, j = 0)$ (index R0 for dominant interface recombination and zero current). ΔE_c can be calculated from $j = j_n + j_p = 0$ with

$$j_n = e \frac{x_m}{\tau_n} (n_{1jR0} - n_{10}) \tag{15a}$$

$$j_p = e s_j n_{1jR0} \tag{15b}$$

yielding (with $n_{2jR0} \approx n_{10}$)

$$\Delta E_c = kT \ln \left\{ \frac{\tau_n}{x_m} \left(s_j + \frac{x_m}{\tau_m} \right) \right\} \tag{14a}$$

This causes a reduction in the open circuit voltage by the same amount or with eqns. (5) and (6) yields

$$V_{oc} \approx \frac{1}{e} E_{g1} - \frac{kT}{e} \ln \left\{ \frac{N_{c1}}{g x_m} \left(s_j + \frac{x_m}{\tau_m} \right) \right\} - \frac{1}{e} (E_{Fp} - E_v) - \frac{1}{e} \delta E_{g1} \tag{16}$$

(Again, we assume a simple[a] current relation for the electron transport through the junction.)

The open circuit voltage given by eqn. (16) is in much improved agreement with the experiment for the CdS–Cu_2S solar cell. (See Section 5.)

[a] In fact, the net electron current through the junction is given as the difference of two current components for electron transfer from the emitter into the junction and in the opposite direction, and each one of these components is the integral of all electron transfers over all energies.

4. Interface recombination and band interconnection

As indicated in Section 3.4 the magnitude of interface recombination will influence the band interconnection between emitter and junction (here discussed for the example of abrupt heterojunction). We shall now discuss such an interface in more detail (for definiteness for the example of a CdS–Cu_2S heterojunction).

In the past interface recombination and the interface discontinuity of the bands were discussed independently [11, 12].

The difference of electron affinities in the two joining materials was used as guidance for the magnitude of the jump of the conduction bands [11]. The value for the interface recombination velocity was estimated from the dislocation density to be of the order of 10^5 - 10^6 cm s^{-1} [12].

However, there is often seemingly contradicting experimental evidence indicating a jump in the conduction bands, and at the same time a spike due to a lowering of the Fermi level, but also evidence for tunneling is observed for CdS–Cu_2S photovoltaic cells [17 - 20, 46 - 51]. Therefore we have in the past refrained from assuming a specific discontinuity [5, 6]. However, as shown in Section 3.4, by assuming major interface recombination a jump of the conduction band edge by ΔE_c (which could be as large as 0.18 eV) is expected at the interface between CdS and Cu_2S.

It is the purpose of this section to analyze the chemistry of this interface layer in order to obtain estimates for the recombination velocity at the CdS–Cu_2S heterojunction and to see what consequences for the band picture near the interface result. This analysis is based on an estimate of the lattice mismatch and the related space charges.

4.1. Mismatch dislocation field

Cu_2S is usually produced on top of a CdS layer by a topotaxial exchange reaction replacing a cadmium ion by two copper ions but leaving the sulfur sublattice essentially intact. The lattice structure changes slightly from the hexagonal CdS with a = 4.1368 Å and c = 6.7162 Å to the orthorhombic chalcocite (Cu_2S) with a = 11.976 Å, b = 27.640 Å, c = 13.488 Å and β = 116.35° (only the elementary cell of the chalcocite lattice is substantially larger than that of the CdS) [13, 14].

The lattices are connected in a plane perpendicular to c (however, because of the surface roughness, a substantial fraction of the interface is along higher index planes [15]). Figure 9 shows a cut through a sulfur layer at the CdS–Cu_2S interface perpendicular to c.

Because of the slight lattice mismatch an interface dislocation field is created with a dislocation spacing of

$$\delta_i = \frac{x_{i1}^2 + x_{i2}^2}{2\Delta x_i} \tag{17}$$

where x_{i1} is the layer distance in ith direction and Δx_i is the mismatch (index 1 or 2 refers to material 1 or 2).

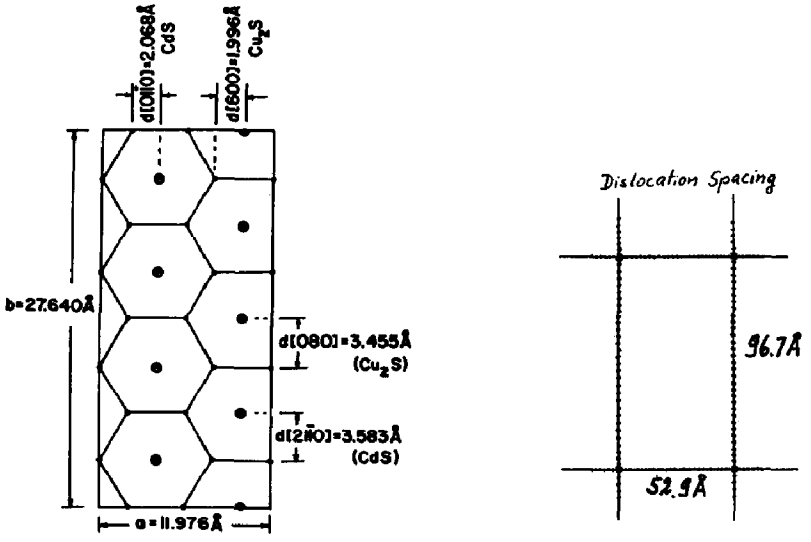

Fig. 9. Cu_2S elementary cell perpendicular to *c* cut (approximate). The sulfur layer is depicted. Lattice mismatch to CdS lattice is indicated.

Fig. 10. Dislocation network at the CdS–Cu_2S interface. Dangling bonds indicated along each dislocation line.

Along each dislocation line, there is one dangling bond for each sulfur atom (Fig. 10), resulting in an interface dangling bond density of

$$D_{ij} = \frac{x_{i1}\Delta x_j + x_{j2}\Delta x_i}{x_{i1}x_{i2}x_{j1}x_{j2}} \tag{18}$$

The dislocation spacing and dangling bond densities for the CdS–Cu_2S basic interfaces are listed in Table 1.

The sulfur dangling bonds represent shallow acceptors which are highly attractive to electrons and will become negatively charged. However, with a density of typically 10^{14} cm^{-2} of these defects, it is immediately seen from the once-integrated Poisson equation that a field jump

$$\Delta F = \frac{e}{\epsilon\epsilon_0} D_{ij} \tag{19}$$

would result which is much too large (10^7 V cm^{-1}) to be permitted. A mechanism to control the effective interface charge at a substantially lower level is therefore required.

4.2. Interface double layer

One possibility to reduce the negative interface charge is by compensation. In the CdS–Cu_2S system such a charge compensation is most easily accomplished by metal ion interstitials (positively charged donors) close to the dislocations.

For reasons of such compensation and for a rather localized stress field [16] near the dislocations, a substantially increased solubility of cadmium

TABLE 1

Lattice parameters of CdS and Cu_2S with interface dislocation field

	CdS	*Cu_2S (orthorhombic)*	
Lattice constant (Å)	(1000) 4.1368	(100) 11.976 (010) 27.640	
	(0001) 6.7162	(001) 13.488	
Lattice spacing as aligned (Å)	$d[2\bar{1}\bar{1}0]$ 2.068 $d[01\bar{1}0]$ 3.583 $d[0002]$ 3.358	$d[600]$ 1.996 $d[080]$ 3.455 $d[004]$ 3.372	
	Interface		
	(100)	(010)	(001)
Lattice mismatch	0.078 Å, 3.6%	0.128 Å, 3.7%	0.013 Å, 0.4%
Dislocation			
Spacing (Å)	52.9	96.7	808.8
SL[a]	26	27	240
Density (cm^{-2})	1.28×10^{11}	2.34×10^{11}	1.95×10^{12}
Orientation	Perpendicular to *a*	Perpendicular to *b*	Perpendicular to *c*
Dangling bond density (cm^{-2})	3.44×10^{13}	6.25×10^{13}	1.07×10^{14}

[a]SL indicates the number of sulfur layers between dislocations.

ions in Cu_2S is expected to accommodate the relatively large (localized) densities of such interstitials:

$$N_M = D_{ij}/d \tag{20}$$

with N_M the density of the metal ion interstitials and d the thickness of the compensating layer.

Assuming a simple Schottky space charge double layer, d can be estimated from

$$d = \left(\frac{2eV_i}{kT}\right)^{1/2} \left(\frac{\epsilon\epsilon_0 kT}{e^2 N_M}\right)^{1/2} \tag{21}$$

resulting in a potential barrier of height

$$V_i = \frac{kT}{e} \ln\left(\frac{N_M}{p_0}\right) \tag{22}$$

with p_0 the density of holes in the adjacent bulk, yielding for N_M the implicit equation

$$D_{ij} = \left\{ 2N_M \frac{\epsilon\epsilon_0 kT}{e^2} \ln\left(\frac{N_M}{p_0}\right) \right\}^{1/2} \tag{21a}$$

and for $D_{ij} = 10^{14}$ cm^{-2}, $\epsilon = 10$ and $p_0 = 10^{19}$ cm^{-3} resulting in $N_M \approx 5 \times 10^{21}$ cm^{-3}, $d \approx 3$ Å and $V_i \approx 0.16$ V. The small thickness of this layer requires the use of a modified dielectric constant, in turn changing N_M and d slightly; hence the rounded-up values here.

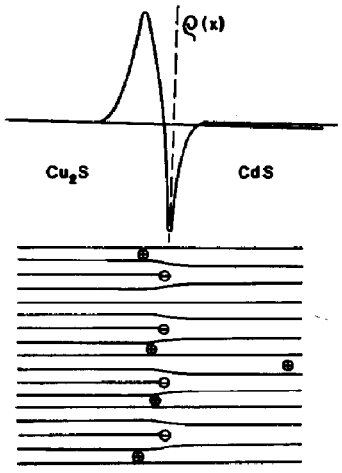

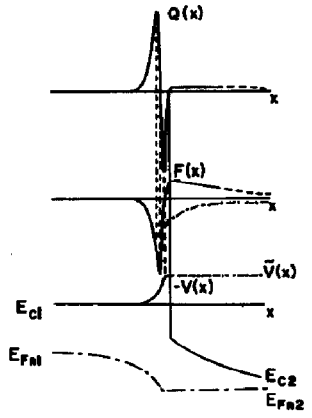

Fig. 11. Space charge distribution. In the lower schematic graph only each sixth layer is depicted.

Fig. 12. Space charge, field and potential distribution near the Cu_2S (left)–CdS (right) heterojunction (shown schematically).

Figure 11 represents a schematic cut through the interface with the resulting space charge distributions. (It also indicates (not to scale) the much lower positive space charge in the junction to the right of the interface double layer.)

The main double layer causes a field distribution shown schematically (chain line to the right of the interface) in Fig. 12. The resulting potential barrier of moderate height (0.16 V in the given example) is given in the lower part of Fig. 12 as a solid curve to the left of the interface and as a chain line to the right of the interface and labeled $\tilde{V}(x)$.

It should be recognized that the estimated density of the cadmium interstitials near the sulfur dangling bonds of the mismatch dislocation field is extremely large. Consequently, we may with some caution speak of an interlayer of Cd_yCu_zS between the CdS and the Cu_2S, which probably has a wider gap than Cu_2S, hence permitting the formation of the potential barrier as shown in Fig. 12.

The formation of such an interlayer, however, renders the estimate of band interconnections using the difference of electron affinities invalid. We will therefore base our estimate on the more fundamental condition of vanishing total current for open circuit condition. As shown in Section 3.4, the total current near the interface must take into consideration substantial interface recombination.

4.3. Interface recombination

The proposed nature of the interface defects, namely cadmium interstitials in very close proximity to sulfur dangling bonds, compensating most of these dangling bonds, renders a large fraction of these donor–acceptor pairs as recombination centers. The interface recombination velocity may be

estimated in a simple homogeneous sheet model (assuming homogeneous distribution of these recombination centers throughout the interface layer) as

$$s_j = v_n q_n N_M d \tag{23}$$

where v_n is the r.m.s. velocity of electrons and q_n the recombination cross section. Assuming $q_n \approx 3 \times 10^{-15}$ cm^2 we obtain $s_j \approx 5 \times 10^6$ cm s^{-1} for a layer perpendicular to c.

The interface recombination lowers the quasi-Fermi level[a] E_{Fn} in Cu_2S (see eqn. (14a)) at the junction interface by

$$\Delta E_{Fn} = kT \ln \left\{ \frac{\tau_n}{x_m} \left(s_j + \frac{x_m}{\tau_n} \right) \right\} \tag{14b}$$

and hence causes a conduction band edge jump of

$$\Delta E_c = \Delta F_{Fn} + eV_i \tag{14c}$$

and is shown in the lower part of Fig. 12 as solid curve $E_c(x)$ (the potential distribution shown in CdS is due to the junction space charge).

The amount of the band edge jump is of the order of 0.34 eV for typical values $\tau_n \approx 2 \times 10^{-9}$ s, $x_m \approx 10^{-5}$ cm and $V_i \approx 0.16$ V.

In conclusion one sees that as a consequence of introducing a sufficiently high density of interface dislocations a substantial charge compensation is necessary, and if such compensation is achieved by a space charge double layer of proper sequence[b] a spike and a jump in $E_c(x)$ is produced (the latter caused by strong interface recombination).

4.4. Influence on short circuit current

The potential spike lowers the short circuit current [8] since electrons diffusing in the conduction band of Cu_2S to the junction interface now have to tunnel through this spike.

Assuming a homogeneous interface sheet with a potential spike of height V_i and effective thickness d_{eff}, the electron transmission t through such a spike can be estimated as

$$t = \exp \{-1.02 \times 10^8 (V_i)^{1/2} d_{eff}\} \tag{24}$$

hence the short circuit current is reduced to

$$j_s = j_{s0} \exp \{-1.02 \times 10^8 (V_i)^{1/2} d_{eff}\} \tag{24a}$$

It is seen that the tunneling current increases with increasing p_0 (since V_i and d decrease with increasing p_0) (Fig. 13). However, one should remember that the minority carrier lifetime decreases with increasing p_0 (see eqn. (8) of

[a] For the open circuit condition depicted.

[b] If the compensating positive charge is to the left (Figs. 11 and 12) of the negatively charged interface.

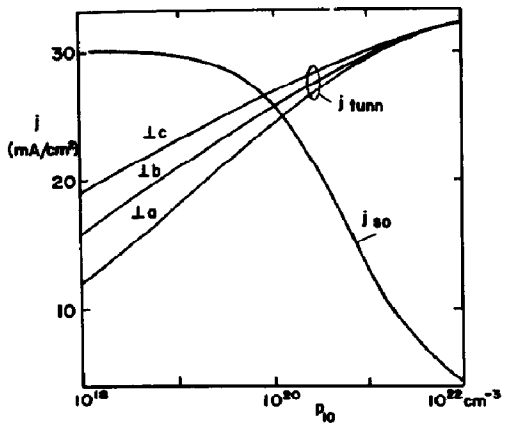

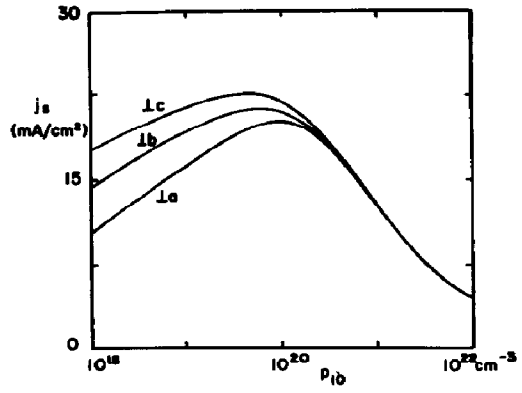

Fig. 13. Tunneling current j_{tunn} through the potential spike at the basic CdS–Cu_2S interfaces and saturation current j_{s0} without such a spike as a function of the acceptor (carrier) density in the Cu_2S bulk.

Fig. 14. Saturation current considering tunneling through the potential spike as a function of the acceptor density in Cu_2S.

ref. 5). Assuming a simple monomolecular recombination, $\tau_n = 1/\gamma p_0$, where γ is the recombination coefficient, eqn. (13e) yields

$$j_{s0} = eg(\mu_n kT/e\gamma p_0)^{1/2} \tanh \{x_m/(\mu_n kT/e\gamma p_0)^{1/2}\} \qquad (13f)$$

as shown also in Fig. 13.

Figure 14 shows a set of resulting curves for the expected short circuit current j_s of eqns. (24a) and (13f) for the three basic interfaces of CdS and Cu_2S (perpendicular to a, perpendicular to b and perpendicular to c). The saturation current through the interface is largest perpendicular to c with the highest density of dislocations. This is caused by the fact that the width of the spike increases with decreasing D_{ik} and dominates in the tunneling expression, even though V_i decreases with decreasing D_{ik}.

The position of the current maximum in Fig. 14 at $p_0 \approx 10^{19} - 10^{20}$ cm^{-3} is valid for the model used. However, the calculated currents are slightly less than those actually obtained in the best CdS–Cu_2S solar cells at AM1 excitation, indicating that the model used is a bit too simplified. (The use of $d_{eff} \approx 0.5d$ partially compensates for this deficiency.)

A better model may contain a more realistic estimate of the shape of the potential spike and an improved expression of the tunneling through such a spike. It should also refer to the fact that the junction interface is not a flat and homogeneous sheet but that the dangling bonds are distributed like a two-dimensional matrix of window frames (Fig. 10), with compensating charges more densely distributed near these frames than along the openings in the center of each frame. This renders the space charge and hence potential distribution three-dimensionally inhomogeneous. Finally, one should take into consideration the higher probability of an electron transition from cadmium interstitials in Cu_2S directly into the conduction band of CdS.

With the limited amount of data available, the discussion of a more complex model has at present little justification. However, additional[a] experimental evidence for the existance of such a potential spike may be obtained from the change of the saturation current in $Cd_zZn_{1-z}S$–Cu_2S cells with changing lattice mismatch caused by variation in z.

4.5. Variation with changing lattice mismatch

With a reduction in lattice mismatch, the density of interface dislocations is reduced; hence the space charge and consequently the height of the potential spike decreases. However, with decreasing space charge, the thickness of the spike will increase (see eqns. (21) and (22)). This will cause a decrease in current as indicated by the tunneling equation and is in qualitative agreement with the experiment. We shall now analyze this behavior in more detail.

The density of dangling bonds in a plane perpendicular to c for the $Cd_zZn_{1-z}S$–Cu_2S interface is given by

$$D_{ik} = \frac{|\tilde{x}_{ik}\Delta x_i| + |\tilde{x}_{1i}\Delta x_k|}{\tilde{x}_{1i}x_{2i}\tilde{x}_{1k}x_{2k}} \tag{18a}$$

where $\Delta x_i = \tilde{x}_{1i} - x_2$, $\tilde{x}_{1i} = x_{3i} + z(x_{1i} - x_{3i})$ and x_{ik} is defined in Table 2. D_{12} is shown as a function of the Zn content in Fig. 15 and has its minimum perpendicular to c for $1 - z \approx 0.466$.

TABLE 2

Definition and values of x_{ik}

	CdS	Cu_2S	ZnS
a	x_{11} $d(2110) = 2.068$ Å	x_{21} $d(600) = 1.996$ Å	x_{31} $d(2110) = 1.912$ Å
b	x_{12} $d(0110) = 3.583$ Å	x_{22} $d(080) = 3.445$ Å	x_{32} $d(0110) = 3.3108$ Å
c	x_{13} $d(002) = 3.358$ Å	x_{23} $d(004) = 3.372$ Å	x_{33} $d(0002) = 3.12$ Å

The thickness and height of the potential spike as function of D_{12} are given by

$$d = 2V_i\epsilon\epsilon_0/eD_{12}(z) \tag{25a}$$

$$V_i = \frac{kT}{e} \ln \{D_{12}(z)\,|p_0 d\} \tag{25b}$$

[a] Additional to the evidence obtained from current–voltage characteristics [17 - 20, 46 - 51].

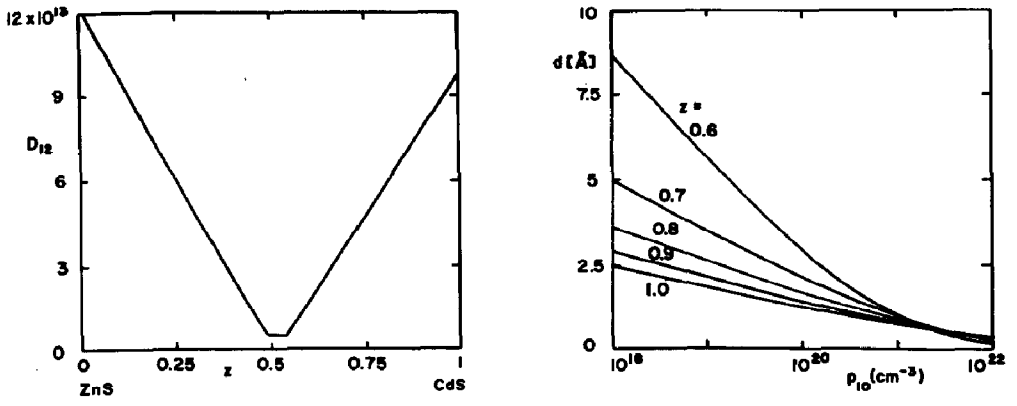

Fig. 15. Density of dangling bonds as a function of Zn content z in $Cd_zZn_{1-z}S$–Cu_2S cells for a plane normal to the c axis.

Fig. 16. Thickness of interface space charge layer as a function of the acceptor density in Cu_2S with composition z of $Cd_zZn_{1-z}S$ layer as family parameter.

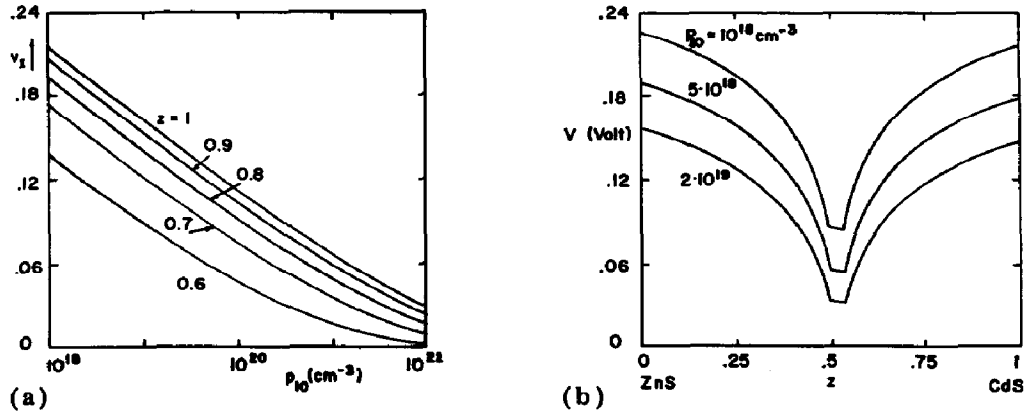

Fig. 17. (a) Height of potential spike as a function of p_{10} with z as family parameter. (b) Height of potential spike as a function of z with p_{10} as family parameter.

and are shown as a function of p_{10} (in Figs. 16 and 17(a)) or as functions of z (Fig. 17(b)). With eqn. (24) one obtains for the current through such a junction as function of the Zn content a set of curves given in Fig. 18 for different values of p_{10} as the family parameter:

$$j_s = j_{s0} \exp\left\{-\frac{1.02 \times 10^8 \epsilon\epsilon_0 V_1^{3/2}(z)}{eD_{12}(z)}\right\} \tag{24b}$$

The transparency of such a potential spike first decreases with decreasing lattice mismatch caused by the widening of the spike. Only when the spike is low enough that most of the electrons can diffuse over it rather than tunneling through it, will the current through such an interface increase again. However, because of the anisotropy of Cu_2S a sufficient match cannot

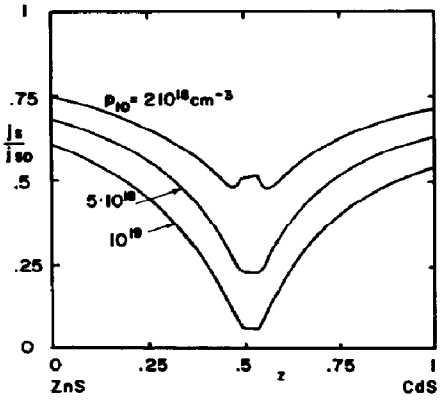

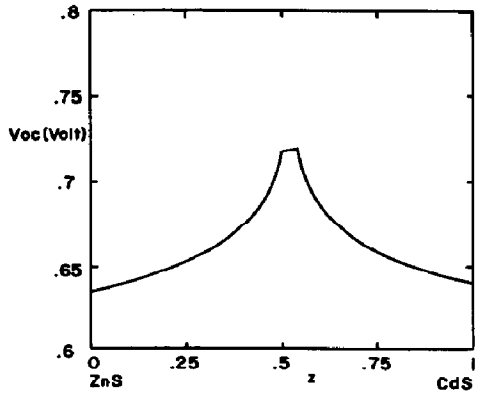

Fig. 18. Current reduced by tunneling through the interface potential spike as a function of the Zn content z in $Cd_zZn_{1-z}S$–Cu_2S cells with hole density p_0 in Cu_2S as family parameter (computed from eqns. (24b), (25a) and (25b) with $\epsilon = 10$).

Fig. 19. Open circuit voltage as a function of composition parameter z computed for $p_{10} = 5 \times 10^{18}$ cm^{-3}.

be achieved with $Cd_zZn_{1-z}S$ (*e.g.* a perfect match in the a direction requires $1 - z = 0.4615$ and in the b direction $1 - z = 0.4705$ leaving at the minimum, with $1 - z = 0.4661$, still a residual dangling bond density of 5.2×10^{12} cm^{-2}); for high densities of p_{10}, Fig. 16 indicates such a current rise. Here V_i has indeed decreased below $2kT$. Figure 18 shows the expected decrease in j_s with decreasing density of interface states.

With decreasing lattice mismatch, *i.e.* also decreasing density of interface recombination centers, however, the open circuit voltage increases (see eqns. (14), (20) and (21)):

$$V_{oc} = \frac{1}{e}E_{g1} - \frac{kT}{e}\ln\left\{\frac{N_{c1}}{gx_m}qv_nD_{12}\right\} - \delta E_{g1} - \frac{1}{e}(E_{Fp} - E_v) \qquad (26)$$

and is shown for $\delta E_{g1} = 0$ in Fig. 19 for $p_{10} = 10^{18}$ cm^{-3} (see Section 5). This seems to explain the often observed fact [21, 22] that with increasing open circuit voltage the short circuit current decreases when the lattice mismatch is reduced (in solar cells with junctions in the collector material). The opposite is true for junctions in the emitter material ($CdTe$–$Cd_zZn_{1-z}S$).

5. Experimental evidence

The theory given provides improved understanding and yields better agreement with the experiment.

(a) The theory is self-consistent and for the description of the current–voltage characteristic does not require the mathematically inacceptable parallel shift of the dark-diode characteristic.

(b) The pre-exponential factor j_{00} in the photovoltaic diode equation is several orders of magnitude lower than about 10^7 A cm^{-2} required by previous

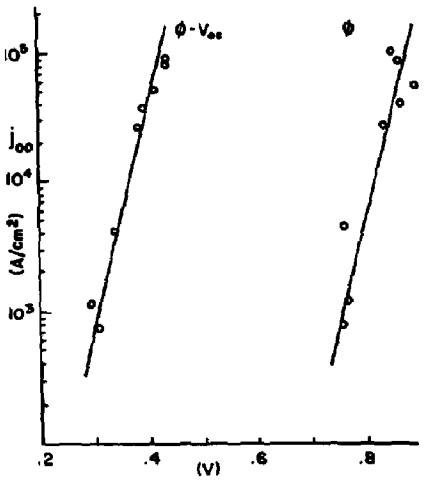

Fig. 20. Pre-exponential factor j_{00} (eqn. (13b)) as a function of ϕ or $\phi - V_{oc}$ (eqn. (26)).

theories. Experimental values lie indeed in the 10^3 - 10^6 A cm^{-2} range (see Fig. 20 and later).

(c) ϕ is not the barrier height but the sum of V_{oc} and the barrier height $\tilde{V}_D$ in agreement with the experiment.

(d) j_{00} and ϕ are connected via τ_n (see eqns. (6), (7) and (13)) resulting in an exponential relation for $j_{00}(\phi)$:

$$j_{00} = eN_{c1}s_j \exp\left(-\frac{E_{g1} - e\phi}{kT}\right) \tag{27}$$

In CdS–Cu_2S solar cells such behavior is indeed measured [23] in good agreement with the experimental slope (Fig. 20) but is shifted by 168 mV towards lower ϕ values (with $N_{c1} \approx 10^{19}$ cm^{-3}, $s_j \approx 5 \times 10^6$ cm s^{-1} and $E_{g1} \approx 1.18$ eV).

This is nearly the same difference between measured and theoretical open circuit voltage as obtained in the set of these cells used for Fig. 20 and calculated from eqn. (16) with $E_{Fp} - E_v + |\delta E_{g1}| = 0$ ($V_{oc}^{(th)} = 614$ mV, $V_{oc}^{(exp)} = 450$ mV). Hence, when j_{00} is plotted against $\phi - V_{oc}$ (Fig. 20) excellent agreement between theory and experiment is observed:

$$j_{00} = egx_m \exp\left\{-\frac{e(\phi - V_{oc})}{kT}\right\} \tag{27a}$$

yielding $gx_m = 4.5 \times 10^{16}$ cm^{-2} s^{-1}, a value within the experimental error expected from excitation (AM1: $g \approx 5 \times 10^{21}$ cm^{-3} s^{-1}) and thickness of Cu_2S (yielding $x_m \approx 10^{-5}$ cm).

This result emphasizes the importance of eqn. (13c). The reason for the shift of V_{oc} is probably related to the rough surface of the CdS–Cu_2S layer [23], accounting for approximately half of the shift, the rest being probably

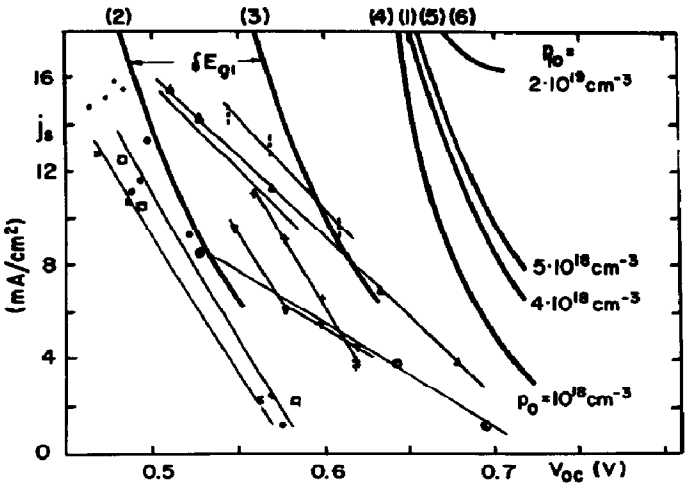

Fig. 21. Short circuit current as a function of open circuit voltage for a variety of polycrystalline $Cd_zZn_{1-z}S$–Cu_2S solar cells (measured points) and theoretical curves (1) - (6) obtained from eqns. (26) and (24b) eliminating D_{12} (see text). For calculating δE_{g1} a value of $N_{c1} = 10^{19}$ cm^{-3} was used.

caused by gap narrowing in the degenerated Cu_yS with $1.99 < y < 1.998$ for typical cells. With a density of copper vacancies (acting as shallow acceptors) of

$$[V_{Cu}] = (2 - y) \times 4.3 \times 10^{22}\ \text{cm}^{-3} \tag{28}$$

we estimate $8.6 \times 10^{18} < [V_{Cu}] < 4.3 \times 10^{20}$ cm^{-3}. Having no other information about band gap narrowing in Cu_2S we may use a highly simplified band-tailing approach with

$$\delta E_{g1} \approx \frac{kT}{e} \ln([V_{Cu}]/N_{v1}) \tag{29}$$

yielding $0 < \delta E_{g1} < 95$ mV for the above given range of y. Hence we expect for multicrystalline CdS–Cu_2S solar cells with rough surfaces a typical range of

$$425 < V_{oc} < 520\ \text{mV} \tag{30}$$

again in good agreement with the experiment.

The increase of V_{oc} with decreasing lattice mismatch for $Cd_zZn_{1-z}S$–Cu_2S solar cells, combined with decreasing short circuit current follows directly from the proposed theory. Figure 21 shows j_{sc} (V_{oc}) as observed [22] for a variety of $Cd_zZn_{1-z}S/Cu_2S$ cells tested in AM1 (100 W cm^{-2} simulated sunlight [24]) condition for various values of z. Cells made with similar fabrication processes are connected by a line, indicating the previously mentioned trend[a] of decreasing j_{sc} with increasing V_{oc}.

[a] Some of the early observation included aggravating factors enhancing this trend, such as decreasing thickness of Cu_2S with increasing z when prepared with disregard of changing topotaxy kinetics.

Figure 21 also contains a set of six theoretical curves (eliminating D_{12}, hence z, from eqns. (25a), (25b) and (24b)). Curve (1) is the solution of eqns. (26) and (24a) for $[V_{Cu}] \approx p_{10}$ and $p_{10} = 3 \times 10^{18}$ cm^{-3}. Curve (2) is shifted in voltage by 170 mV and curve (3) is shifted by 90 mV[a] from curve (1) indicating a range between these curves expected by band gap narrowing (δE_{g1}) in Cu_yS for a variation in stoichiometry in the range $1.99 < y < 2$. This theoretical range shows reasonable agreement with the experiment. The other three curves are similar to (1), but have different values of p_{10} (as given as family parameters).

For the experimental points, the range of Zn content covered in Fig. 21 is from 0 to about 40% and shows considerable scatter dependent on the preparation of the cell [22].

In contrast, the shift of ϕ, as defined by

$$j = j_{00} \exp\left(-\frac{e\phi}{kT}\right) \exp\left(\frac{eV}{kT}\right) - j_{sc} \tag{30}$$

with V_{oc} as observed (after correcting for j_{sc} ([22]), indicates a maximum open circuit voltage when $e\phi \approx E_{g1}$, yielding V_{oc} (max) ≈ 0.75 V[a]. From Fig. 5 in ref. 25, we extrapolate that at a Zn-content between 40 and 50%, such a V_{oc} value may indeed be achieved, as predicted by the given theory with minimum mismatch near 47%.

6. Consequences for design of efficient solar cells

The theory described in Sections 3 and 4 of this presentation and compared with experimental results, obtained from CdS–Cu_2S or $Cd_zZn_{1-z}S$–Cu_2S solar cells, may be used to predict possible performance of various materials or material combinations as solar cells. A short overview of the main steps for such an evaluation will now be given. We shall follow the outline of the different parts of the cell given in Section 2.

6.1. Emitter

(a) The emitter must absorb a major fraction of the solar radiation within its thickness d_1.

(b) The generated minority carriers must have a sufficient lifetime–mobility product to provide a diffusion length of at least $2d_1$.

(c) Outer surface recombination must be low enough to permit collection of more than half the generated minority carriers at the junction.

[a]The remaining shift of about 90 mV is probably due to the rough surface topography in polycrystalline cells [8, 23].

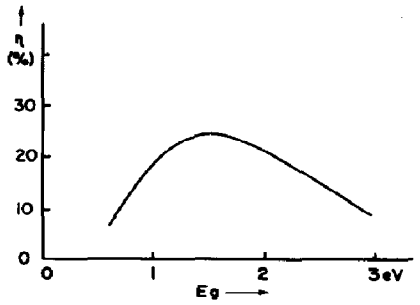

Fig. 22. Maximum theoretical efficiency of solar cells as a function of the band gap energy of the emitter material.

(d) The minority carrier lifetime must be high enough to permit the development of a sufficient open circuit voltage.

(e) The band gap must be high enough to permit a sufficient open circuit voltage, but low enough to have most of the sunlight absorbed in the emitter.

These conditions have been discussed in the past and are summarized in the classical literature on limit efficiencies, reprinted in ref. 26 (see also refs. 27 - 32).

The most significant results are given in Fig. 22 showing maximum achievable efficiencies with emitter materials of a band gap near 1.5 eV. Table 3 shows a list of some materials ordered by increasing distance from $E_g \approx 1.5$ eV.

Factors entering the selection of an emitter material are direct *versus* indirect band gap material — the latter having much smaller optical absorption, hence requiring thicker material and consequently better quality material for reasons of a much longer diffusion length to bridge the thickness of this material.

When interface recombination can be neglected, the larger minority lifetime (due to a larger diffusion length) is beneficial also for a larger open circuit voltage (eqn. (16)). With major interface recombination, however, this consideration is no longer valid (eqn. (26)).

Indirect band gap material shows increased optical absorption with increased defect density, probably at densities above 10^{19} cm^{-3}. Cu_xS seems to be an example of this behavior. Increased defect density also reduces the minority carrier life. Fine tuning to achieve an optimum between these detrimental and beneficial influences is required. Too little is known presently to make quantitative estimates.

p-type material is preferable for emitters over n-type material, since μ_n is usually larger than μ_p and hence the diffusion length of minority electrons is expected to be larger than that of holes.

The ease of producing large layers of this material with easily controllable doping is an important factor in manufacturing inexpensively efficient cells. Homogeneity is necessary to avoid detrimental internal currents caused by parallel connection of parts of the cell with different electrical properties.

TABLE 3

Possible emitter materials

Material	Band gap at 300 K (eV)	Gap transitive	Mobility at 300 K		Static dielectric constant	Lattice constant (Å)			Thermal expansion coefficient at 300 K	Preferred[a] conduction type
			Electron	Hole		*a*	*b*	*c*		
1. Elements										
Si	1.11	indirect	1350	480	12	5.431			2.33×10^{-6}	n, p
Ge	0.66	indirect	3600	1800	16	5.658			5.75×10^{-6}	n, p
Se										
Te										
2. Binary compounds (AB)										
CdTe	1.44	direct	700	65	9.6	6.477				n, p
GaAs	1.43	direct	5 - 8000	300	11.5	5.654			5.8×10^{-6}	n, p
AlSiO	1.6	indirect	280	–	10.1	6.136			3.7×10^{-6}	n, p
CdSe	1.7	direct	100	–	9.6	4.298			4.8×10^{-6}	n
InP	1.27	direct	4500	100	12.1	5.869			4.5×10^{-6}	n, p
AlAs	2.15	indirect	280	–	10.1	5.661			5.2×10^{-6}	n, p
GaP	2.25	indirect	300	150	8.4	5.451			5.3×10^{-6}	n, p
ZnTe	2.26	direct	530	130	10.1	6.103			8.2×10^{-6}	p
CdS	2.45	direct	340	–	10	4.137		6.716	4×10^{-6}	n
GaSb	0.68	direct	5000	1000	14.8	6.095			6.9×10^{-6}	n, p
ZnSe	2.67	direct	530	–	9.1	5.667			7×10^{-6}	n
ZnS	3.58	direct	120	–	8.3	3.814			6.3×10^{-6}	n
InAs	0.36	direct	30000	450	12.5	6.058			4.5×10^{-6}	n, p
PbTe	0.29	indirect	2500	1000	17.5	6.52				n, p
InSb	0.17	direct	80000	450	15.9	6.419			4.9×10^{-6}	n, p

2a. Binary compounds										
Zn_3P_2	1.4	direct		30	10	8.09		11.45	14×10^{-6}	p [34]
Bi_2S_3	1.3									
Cu_2S	1.18	indirect	30	5		11.976	27.64	13.488		p
Cu_2O	1.95	direct								p
In_2Te_3	1.1									
3. Ternary compounds										
$CuInS_2$	1.55	direct	320	10		5.782	–	11.62		n, p [35]
$CuInSe_2$	1.03	direct	200	15		5.523	–	11.12		n, p [35]
$CuInTe_2$	0.96	direct	200	–		6.179	–	12.36		n [35]

[a]Ref. 33, except when stated otherwise.

6.2. Junction

The emitter material must permit the creation of a junction, or must be able to join without excessive mismatch an appropriate n-type material (for p-type emitters).

The junction material must have a low enough density of defect states which will become charged in the junction region. In contrast to the occasionally voiced opinion [11, 12, 36], compensation is often not sufficient [6], since electrons transferred from donors to acceptors with compensation are usually redistributed with optical excitation and still cause major space charges in the junction with carrier depletion.

There are two major possibilities to avoid excessive space charges (hence excessive fields which would cause reverse tunneling, therefore inferior junction behavior):

(a) substantial purification of the junction, or

(b) field-quenching, causing the field to empty also oppositely charged defects, hence reducing the space charge before fields sufficient for excessive tunneling are reached [5, 6].

Lattice mismatch and space charge limitation are the two major conditions (others will be indicated below) to obtain desirable junctions. The present theory does not permit precise limits to be given. However, from the previous discussion it is deduced that there may be two ranges for permissible mismatch:

(a) below a dangling bond density of about 10^{12} cm^{-2} providing a barrier of insufficient height to block currents; and

(b) near a density of 10^{14} cm^{-2} where the windows in the dislocation field open up; however, the spacing of the "window frames" is still wide enough to permit electron transmission through the windows without recombination via donor–acceptor pairs located along these window frames.

Figure 23 shows a comparison of lattice parameters for a variety of binary and ternary semiconducting compounds for obtaining first indications of possible mismatch. However, a more detailed analysis is necessary (proper interface analysis) to obtain valid estimates.

Other desirable parameters of the junction material include sufficient band gap (not less than the gap of the emitter) and minority carrier life to maintain the spread of quasi-Fermi levels from the emitter well into the junction in order to avoid V_{oc} reduction. This necessitates sufficient optical excitation of the junction material and limited recombination here.

6.3. Collector

Junctions and collector must be of compatible (or of the same) materials and must have sufficient (usually n-type) conductivity to avoid excessive series resistance losses. Ease of deposition (fabrication) of the collector layer and avoidance of materials (impurities) with excessive diffusivity into junction and emitter resulting in cell degradation are often items for consideration.

However, compared with much more critical conditions for selection of emitter and junction materials, the collector material selection is far less sensitive.

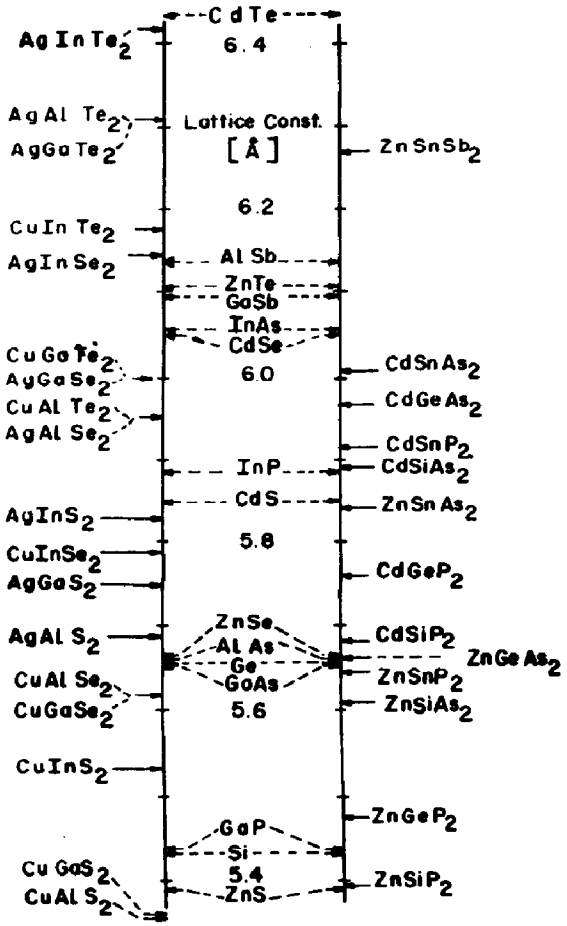

Fig. 23. Comparison of lattice parameter for a variety of binary and ternary semiconducting compounds; see also ref. 52.

6.4. Materials conclusion

From the above discussion it may be concluded that a large variety of materials and material combinations may be candidates for efficient solar cells with only very few yet explored — most prominently Si, GaAs and Cds–Cu_2S. The recent discovery of other cells with efficiencies in excess of 5%, such as CdS–InP (12% [37]), CdS–CdTe (7% [38]), In_xSn_y O–InP (6% [39]), CdS–$CuIn_2Se$ (6.7% [40], single crystal 10%, [41]), Si_xH ("amorphous Si" 5.5% [42]) Si–SnO_2 (10% [43] and Zn_2P_3 (5% [44]) seem to indicate that indeed many more cell materials may be possible candidates.

However, many factors have to come together to make such candidates attractive for large scale inexpensive production. These include availability of sufficient quantities of raw material, inexpensive purification and deposition methods, easy process control to achieve a large area product within acceptable performance tolerances and a high life expectancy of the finished solar cell.

Presently only a few materials qualify as candidates for such development. However, it is too early to make substantial predictions about the possible development in this field of great potential for large scale solar energy conversion.

7. Summarizing remarks

The commonly used parallel shift of a diode characteristic by the short circuit current is mathematically only permissible in a small range near the open circuit voltage [6]. This can be shown by connecting the diffusion current of minority carriers in the emitter with the voltage drop calculated by integrating the transport equation of the same carriers in the junction in the Boltzmann range, and using the electron density n_j at the interface between emitter and junction as the connecting boundary condition. This means that n_j determines j_n in the emitter (eqn. (4)) and it determines the voltage drop in the junction (eqn. (11a)) when the junction is emitter controlled[a] [45]. This remains the case also outside the Boltzmann range; however, it necessitates proper integration of the transport and Poisson equations. The solutions then become space charge dependent, determining the shape of the current–voltage characteristics.

The analysis near the open circuit condition provides insight into the transport mechanism through the junction interface. A moderate reduction of the open circuit voltage is observed if major interface recombination takes place. This causes a band edge jump of the same magnitude (as the reduction of V_{oc}). Such a band edge jump modifies the jump often assumed in heterojunctions and previously estimated from the differences in electron affinities, although in disregard for the chemistry of the interface layer; it removes the difficulties encountered in earlier models when discussing vanishing currents for open circuit conditions.

In addition to the jump a potential spike is encountered when major lattice mismatch forces the creation of a space charge double layer at the interface. This spike causes a reduction of the short circuit current which is almost negligible at high space charge densities (ease of tunneling). With decreasing mismatch the current first decreases as the spike widens and increases only when the spike becomes negligible at a mismatch of probably[b] substantially less than 1% (however, as shown in Section 4.5, the defect density in the emitter has major influence on the permissible mismatch). The agreement obtained between theory and experiment encourages the pursuit of a more detailed analysis.

---

[a] The theory developed here does not apply without major modifications to collector controlled cells, where most of the junction is located in the emitter. Because of the highly asymmetric doping of solar cells (the front layer must be highly conductive to carry the large lateral current densities to the electrode grid) backwall cells are usually collector controlled (Si cells are an example of such) [45].

[b] The theory presented is too general to permit a better estimate at this time.

Acknowledgments

This work was supported by SES, Inc., and, related to material presented in Section 4, through an invitation to the author to work at the University of New South Wales during late fall 1977. Stimulating discussions with Professor Hora and Dr. Womac are gratefully acknowledged.

References

1 P. A. Crossley, G. T. Noel and M. Wolf, Final Rep. NASA AED-R3346 (1968).
2 A. L. Milnes and D. L. Feucht, Heterojunctions and Metal Semiconductor Junctions, Academic Press, New York, 1972.
3 A. Rothwarf and K. W. Böer, Prog. Solid State Chem., 10 (1975) 71.
4 R. Hill, in T. J. Coutts (ed.), Thin Film Solar Cells in Active and Passive Thin Film Devices, Academic Press, London, 1978.
5 K. W. Böer, Phys. Rev., B13 (1976) 5373.
6 K. W. Böer, Proc. 12th IEE Photovoltaic Specialists Conf., Baton Rouge, 1976, p. 475.
7 K. W. Böer, Proc. El. Chem. Soc. Atlanta, Ga., 1977.
8 K. W. Böer, Proc. Int. Solar Energy Soc., New Delhi, 1978, Pergamon Press, Oxford.
9 K. W. Böer, Phys. Status Solidi A, 40 (1977) 355.
10 E. Spenke, Electronic Semiconductors, Springer-Verlag, Berlin, Heidelberg, New York, 1965.
11 L. R. Shiozawa, G. A. Sullivan and F. Augustine, Proc. 8th IEEE Photovoltaic Specialists Conf., 1968, p. 39.
12 A. Rothwarf, Proc. Int. Conf. on Solar Electr., Toulouse, France, 1976.
13 M. T. Evans, Jr., Nature (London) Phys. Sci., 232 (1971) 69.
14 R. W. Potter and M. T. Evans, Jr., United States Geological Survey, 1975.
15 K. A. Jones, J. Crystal Growth, 43 (1978) 165.
16 M. J. Marcinkowski and W. F. Tseng, Metall. Trans., 1 (1970) 3397.
17 W. D. Gill and R. H. Bube, J. Appl. Phys., 41 (1970) 1694.
18 P. F. Lindquist and R. H. Bube, J. Appl. Phys., 43 (1972) 2839.
19 F. Pfisterer, G. H. Hewig and W. H. Bloss, Proc. 11th IEEE Photovoltaic Specialists Conf., 1975, p. 460.
20 S. Martinuzzi and O. Mallem, Phys. Status Solidi A, 16 (1973) 339.
21 W. Palz, J. Besson, T. Nguyen Duy and J. Vedel, Proc. 10th IEEE Photovoltaic Specialists Conf., 1973, p. 69.
22 Progress Rep. ERDA A(49-18)-2538 PRT 6/1, Jan. 1977, IEC, University of Delaware.
23 Semi-Annual Report, NSF/RANN/AER72-03478A04PR75/4, National Science Foundation, U.S.A., 1975.
24 K. W. Böer, Sol. Energy, 19 (1977) 525.
25 L. C. Burton, B. Baron, W. Devany, T. L. Hench, S. Lorenz and J. D. Meakin, Proc. 12th IEEE Photovoltaic Specialists Conf., 1976, p. 526.
26 C. E. Backus, (ed.), Solar Cells, IEEE Press, New York, 1976.
27 J. J. Loferski, J. Appl. Phys., 27 (1956) 777.
28 M. B. Prince, J. Appl. Phys., 26 (1955) 534.
29 J. J. Wysocki and P. Rappaport, J. Appl. Phys., 31 (1960) 571.
30 M. Wolf, Proc. IRE, 48 (1960) 1246.
31 W. Shockley and H. J. Queisser, J. Appl. Phys., 32 (1961) 510.
32 M. Wolf, Energy Convers., 11 (1971) 63.
33 A. G. Milnes and D. L. Feucht, Heterojunctions and Metal–Semiconductor Junctions, Academic Press, New York, 1972.

34 A. Catalano, *et al.*, Proc. Photovoltaic Solar Energy Conf., R. Reidel Publ. Co., Dordrecht, Holland, 1977, p. 644.
35 L. L. Kazmerski, *et al.*, Proc. 12th IEEE Photovoltaic Specialists Conf., 1976, p. 534.
36 L. R. Shiozawa, F. Augustine, G. A. Sullivan, J. M. Smith and W. R. Cook, Clevite Corp. Final Rep. U.S. Air Force AF, 33 (615) (1969) 5224.
37 J. L. Shay, M. Bettini, S. Wagner, K. J. Bachman and E. Buehler, Proc. 12th Photovoltaic Spectroscopy Conf., 1976, p. 540.
38 A. L. Fahrenbruch, *et al.*, Proc. 13th Photovoltaic Specialists Conf., 1978, p. 281.
39 H. M. Manasevit, R. H. Bube, *et. al.*, Proc. 13th Photovoltaic Specialists Conf., 1978, p. 165.
40 L. L. Kazmerski and P. J. Ireland, Proc. 13th Photovoltaic Specialists Conf., 1978.
41 S. Wagner, J. L. Shay, K. J. Bachman and E. Buehler, Appl. Phys. Lett., 26 (1975) 229.
42 D. E. Carlson, C. R. Wronski, A. R. Triano and E. E. Daniel, Proc. 12th Photovoltaic Specialists Conf., 1978, p. 893.
43 J. S. Franz, G. Kent and R. L. Anderson, Symp. on Solar Energy Conversion, Electron. Mater., (1976).
44 A. Catalano, *et. al.*,Proc. 13th Photovoltaic Specialists Conf., 1978.
45 K. W. Böer, Proc. Am. Sect. of ISES Annual Meeting, 2.2, 1978, p. 327.
46 A. E. van Aerschodt, J. J. Capart, K. H. David, M. Fabriocotti, K. H. Heffels, J. J. Loferski and K. K. Reinhartz, IEEE Trans. Electron Devices, ED-18 (1971) 471.
47 A. L. Fahrenbruch and R. H. Bube, J. Appl. Phys., 45 (1974) 1264.
48 T. S. teVelde, Solid State Electron., 16 (1973) 1305.
49 S. Martinuzzi, O. Mallem and T. Cabot, Phys. Status Solidi A, 36 (1976) 227.
50 K. W. Böer and J. Phillips, Proc. 9th IEEE Photovoltaic Specialists Conf., 1972, p. 125.
51 A. Rothwarf and K. W. Böer, Prog. Solid State Chem., 10 (1975) 71.
52 J. L. Shay, S. Wagner, K. Bachman, E. Buehler and H. M. Kasper, Proc. 11th IEEE Photovoltaic Specialists Conf., 1975, p. 503.